

Transient Method for Convective Heat Transfer Measurement over Rough Surfaces with Lateral Conduction

J. Bons

Associate Professor

Brigham Young University

Abstract

The effect of lateral conduction on convective heat transfer measurements using the transient infrared technique over a rough surface is evaluated. Comparisons are made between a full 3-D finite volume analysis and a simpler 1-D transient conduction model. The randomly rough surface is a scaled model of actual surface deposits generated in a gas turbine flowfield. The surface temperature time history was measured with a high resolution infrared camera during an impulsively started hot gas flow over the rough test plate at a flow Reynolds number of 750,000. The boundary layer was turbulent with the peak roughness elements protruding just above the boundary layer momentum thickness. The 1-D model underestimates the peak to valley variations in surface heat flux by up to a factor of five compared to the 3-D model with lateral conduction. For the area-averaged surface heat flux, the 1-D model predicts higher values than a 3-D model for the same surface temperature history. This is due to the larger surface area of the roughness peaks and valleys in the 3-D model which produces a larger initial input of energy at the beginning of the transient. For engineering purposes, where the net heat load into the solid is desired, this lower 3-D model result must be multiplied by the wetted to planform surface area of the roughness panel. For the roughness model in this study, applying this correction results in a 50% increase in the roughness-induced Stanton number augmentation for the 3-D rough surface model compared to a flat 1-D surface model at the same Reynolds number. Other shortcomings of the transient method for rough surface convective heat transfer measurement are identified.

Nomenclature

A – finite volume cell surface area	η_{fc} – film cooling effectiveness
Bi – Biot number ($h_c l / \kappa$)	ν – kinematic viscosity
Fo – Fourier number ($\alpha t / l^2$)	θ – local surface angularity
H(t) – Heaviside function	ρ – density
Γ^+ – surface radiosity	τ – dummy time integration variable
L – distance from leading edge to roughness panel in wind tunnel	ω – frequency of sinusoidal temperature variation
Q – heat flux	
Re _L – Reynolds number ($U_\infty L / \nu$)	<u>subscripts</u>
S – roughness panel surface area	coolant – coolant property
St – Stanton Number, $h_c / (\rho c_p U_\infty)$	flat – planform (flat) surface area
T – temperature	fluid – fluid property
U – velocity	i – summation index
V – cell volume	– x direction cell index
	init – initial condition (t=0)
c_p – specific heat at constant pressure	j – y direction cell index
dt – time step	k – z direction cell index
d ω – differential solid angle	n – summation limit
h_c – convective heat transfer coefficient	– time index
l – panel thickness	s – solid surface adjacent to fluid
q – heat flux per unit area	scond – conductive surface heat flux
t – time	sconv – convective surface heat flux
x – direction into solid from surface	smax – maximum surface temperature in sinusoidal temperature variation
y – upstream direction along surface	srad – radiative surface heat flux
z – crossstream direction along surface	wet – wetted surface area
	∞ – freestream value
α – thermal diffusivity ($\kappa / \rho c_p$)	
Δx – cell dimension in x-direction	
Δt – time step	
κ – thermal conductivity	

Introduction/Background

The accurate measurement of convective heat transfer between a moving fluid and an adjacent solid is a subject of enduring engineering interest. Measurements are most commonly made in the steady-state mode, with either the surface temperature or surface heat flux prescribed while the other is measured to compute the local convective heat transfer coefficient [$h_c = q_s / (T_\infty - T_s)$] at a given fluid temperature (T_∞). Unfortunately, accurate steady-state measurements require careful accounting of conduction and radiative losses and often necessitate meticulously designed arrays of thin-foil surface heaters and associated “guard heaters” to approximate the prescribed wall boundary condition [Hosni et al., 1991]. One option for avoiding some of these complicating factors is by employing the mass transfer analog through steady state techniques such as naphthalene sublimation [Chen and Goldstein, 1991] and pressure sensitive paints [Gao et al., 2005], though these techniques require their own level of sophistication. Another option for accurate h_c measurement is commonly referred to as the “transient” heat transfer method. Transient measurement techniques are a low-cost, efficient alternative that can produce accurate heat transfer measurements with a much shorter test time. These techniques are especially well-suited for transient test facilities (e.g. shock tubes or blow-down type wind tunnels).

Transient techniques have been employed for over half a century in fields as far ranging as hypersonics [Powell and Bons, 2001] and solar collectors [Roger, 2007]. In particular, they have seen broad application in the gas turbine industry for cooled turbine blade design [Bunker, 2004], analysis [Nasir et al, 2004, and Ou and Rivir, 2006], and post-production testing [Nirmalan et al., 2002]. The critical measurement in the transient convective heat transfer method is the time history of surface temperature relative to some impulsively started flow event. The surface temperature can be measured either optically or through standard contact methods (e.g. surface thermocouple arrays) [Walker et al., 2000]. The two most common optical methods include liquid crystals and infrared imaging. Temperature-sensitive liquid crystals can be painted onto any smooth surface and calibrated in-situ. The encapsulated crystals emit visible bands of color at prescribed temperatures. The surface color time history can be imaged with a common CCD camera, at higher resolution and much lower cost than an infrared camera. There are, however, several drawbacks to the liquid crystal technique [Lin and Wang, 2000]. Because the crystals are embedded into the surface coating, they are not located precisely at the surface nor are the thermal properties of the paint necessarily the same as those of the substrate. In

addition, the temperature sensitivity of the crystals is not always in a convenient range (typically very near room temperature). Also, the color bands provide information as to the local time delay for the surface to change from the isothermal (flow off) condition to the temperature associated with the particular color band. Infrared measurement, on the other hand, provides a continuous surface temperature history. This necessitates a different analytical processing technique, as outlined below. Finally, and perhaps most important for this study, liquid crystals are difficult to apply uniformly over rough surfaces. A non-uniform crystal distribution can create significant problems in interpreting heat transfer results. Even standard steady-state measurement techniques are challenged by rough surfaces due to the difficulty of insuring a uniform surface heat flux or wall temperature condition (Bogard et al., 1998, and Hosni et al., 1991). As such, the subject of this study is the application of infrared thermography to the transient measurement of convective heat transfer over a rough surface.

Analytical Development

The essential foundation of the transient heat transfer technique is the unsteady conduction equation. With the assumption of constant thermal properties and no heat generation, this equation can be written in Cartesian coordinates as:

$$\frac{\partial^2 T}{\partial x^2} + \frac{\partial^2 T}{\partial y^2} + \frac{\partial^2 T}{\partial z^2} = \frac{1}{\alpha} \frac{\partial T}{\partial t} \quad [\text{Eq. 1}]$$

or in one-dimension only,

$$\frac{\partial^2 T}{\partial x^2} = \frac{1}{\alpha} \frac{\partial T}{\partial t} \quad [\text{Eq. 2}]$$

The transient technique employs classical solutions to this equation for the specific case of a semi-infinite solid with uniform initial temperature. These initial and boundary conditions are explicitly stated as:

$$T(x,0) = T_{init} \quad \text{and} \quad \lim_{x \rightarrow \infty} T(x,t) = T_{init} \quad [\text{Eq. 3}]$$

Numerous heat transfer texts contain the solution of these equations for two of the most common cases [Mills, 1992, and Kakac and Yener, 1992]:

i) step change in surface temperature: $T(x = 0, t > 0) = T_s$

$$\text{Solution: } \frac{T(x,t) - T_{init}}{T_s - T_{init}} = \text{erfc } \eta \quad \text{where } \eta = \frac{x}{2\sqrt{\alpha t}} \quad [\text{Eq. 4}]$$

ii) step change in fluid temperature: $T_{fluid}(t > 0) = T_\infty$ where $T_{fluid}(t \leq 0) = T_{init}$

$$\text{Solution: } \frac{T(x=0,t) - T_{init}}{T_\infty - T_{init}} = 1 - \exp \beta^2 \text{erfc } \beta \quad \text{where } \beta = \frac{h_c}{\kappa} \sqrt{\alpha t} \quad [\text{Eq. 5}]$$

Since the governing equation (Eq. 2) is linear, an arbitrary $T_s(t)$ or $T_\infty(t)$ distribution can be approximated as the summation of a series of steps, for example:

$$T_s(t) \cong T_{init} + \sum_{i=1}^n [T_s(\tau_i) - T_s(\tau_{i-1})] H(t - \tau_i) \quad [\text{Eq. 6}]$$

where τ is a dummy time variable such that $\tau_0 = 0 < \tau_1 < \dots < \tau_{n-1} < \tau_n = t$ and $H(t)$ is the Heaviside step function, $H(t) = 1$ for $t \geq 0$ and $H(t) = 0$ for $t < 0$. Using Duhamel's superposition theorem, the general solution of Eq. 2 for the boundary condition shown in Eq. 6 is [Kakac and Yener, 1992]:

$$T(x,t) \cong T_{init} + \sum_{i=1}^n [T_s(\tau_i) - T_s(\tau_{i-1})] \Phi(x,t - \tau_i) \quad [\text{Eq. 7}]$$

where $\Phi(x,t) = \text{erfc}(\eta)$, the single step solution from Eq. 4. For the transient liquid crystal technique, the summation (Eq. 6) is specified for T_∞ rather than T_s , and the corresponding Φ function in Eq. 7 is Eq. 5. Since liquid crystals do not emit continuously during the thermal transient, the acquired data consists of local $(T, \Delta t)$ pairs containing the temperature of crystal emission and the delta time from startup that the emission is first visible. With the delta time and T_s known, the h_c can be calculated directly using Eq. 5 (for a single step change in T_∞) or Eq. 7 (for a continuous series of step changes in T_∞).

For the single T_s step transient IR technique employed in this study, Eq. 4 can be differentiated with respect to x at the surface to compute $q_s(t)$:

$$q_s(t) = -\kappa \left. \frac{dT_s}{dx} \right|_{x=0} = \frac{\kappa}{\sqrt{\pi\alpha}} \frac{(T_s - T_{init})}{\sqrt{t}} \quad [\text{Eq. 8}]$$

Or in the case of the temperature step series (Eq. 6), Cook and Felderman [1966] and later Schulz and Jones [1973] derived the following expression (note the similarity to Eq. 8):

$$q_s(t) = \frac{\kappa}{\sqrt{\pi\alpha}} \sum_{i=1}^n \frac{T_s(\tau_i) - T_s(\tau_{i-1})}{2 \left[\sqrt{t - \tau_i} - \sqrt{t - \tau_{i-1}} \right]} \quad [\text{Eq. 9}]$$

That this approximate method accurately predicts the surface heat flux for a time-varying $T_s(t)$ distribution can be verified using the analytical solution for a sinusoidal surface temperature, $T_s(t) = T_{\text{init}} + (T_{\text{smax}} - T_{\text{init}})\sin\omega t$. The analytical solution obtained by separation of variables yields [Mills, 1992]:

$$q_s(t) = \kappa(T_{s \text{ max}} - T_{\text{init}}) \sqrt{\frac{\omega}{2\alpha}} \{ \sin(\omega t) + \cos(\omega t) \} \quad [\text{Eq. 10}]$$

Figure 1 shows a comparison between the analytical $q_s(t)$ solution (Eq. 10) and the approximate solution (Eq. 9) for a step size of $dt = 0.01 \left(\frac{2\pi}{\omega} \right)$. Note the initial startup transient occurs because the analytical solution is valid for all time whereas the approximate method is valid for the $T_s(t)$ variation after $t=0$ only. Thus, at $t=0$, the approximate $q_s = 0$ while the exact (analytical) $q_s > 0$. After the startup transient has died away, the two solutions are essentially identical.

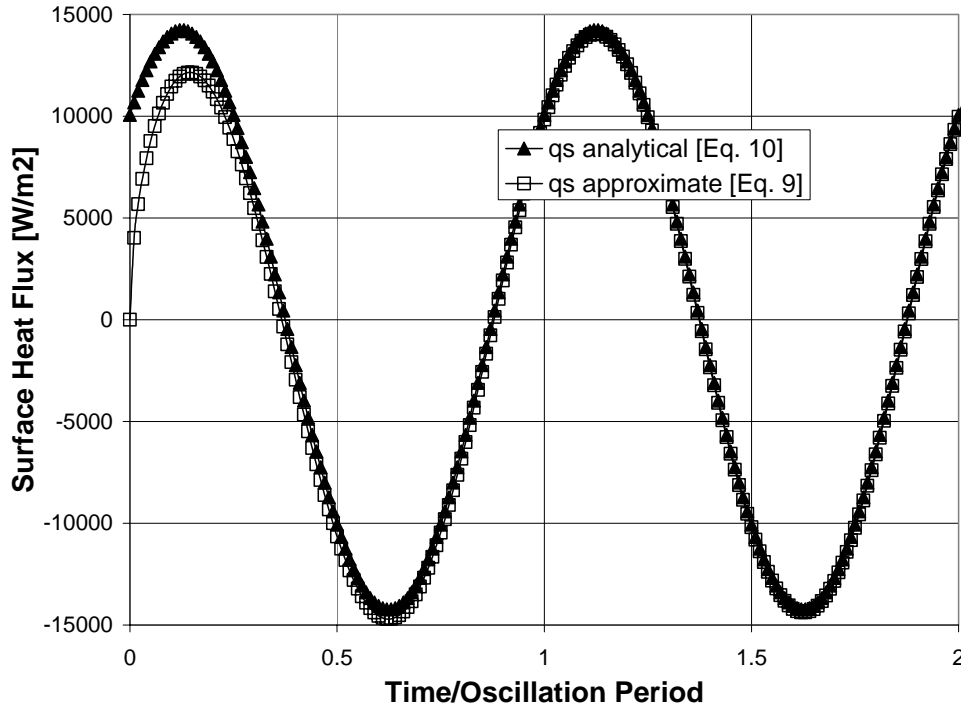


Figure 1: Surface heat flux time history for sinusoidally varying surface temperature. Analytical solution (Eq. 10) vs. approximate summation solution (Eq. 9).

Once the $q_s(t)$ distribution is calculated using Eq. 9, the transient IR method relies on an energy balance evaluated at the surface ($q_{sconv} = q_{srad} + q_{scond}$) to calculate the convected heat flux to the surface (q_{sconv}). The heat transfer coefficient is then computed as $h_c = q_{sconv}/(T_\infty - T_s)$, where q_{sconv} , T_∞ , and T_s are all functions of time in the most general case.

Finite Volume Method for Lateral Conduction

The subject of this paper is the transient IR technique accounting for lateral conduction on non-uniform (rough) surfaces. Since the method outlined above is only valid for 1-D conduction, a finite volume discretization of the solid was employed. The 1-D results are then used as a benchmark for comparison to assess the importance of lateral conduction for a typical rough surface topology. Since the 1-D analysis is simpler to execute, there is a significant cost savings in terms of computational time. Other researchers have employed finite element analyses in conjunction with steady state [Brauckmann and von Wolfersdorf, 2005, and Baldauf et al, 2001] and transient [Nirmalan et al., 2002, and Ling et al., 2004] heat transfer techniques to improve measurement accuracy in regions of steep surface temperature gradients. For example, Ling et al. [2004] measured film cooling effectiveness (η_{fc}) using the transient liquid crystal technique. They compared results obtained from both 1-D and 3-D conduction models and found that in the region just downstream of the film cooling hole, the 1-D model underpredicted η_{fc} by up to 0.25 (a significant difference given that the possible range of values for η_{fc} is only 0 to 1). The authors proposed a criterion to assess the importance of lateral conduction based on Eq. 1. Lateral conduction can be neglected if both of the following conditions are satisfied:

$$\frac{\partial^2 T}{\partial y^2} \ll \frac{1}{\alpha} \frac{\partial T}{\partial t} \quad \text{and} \quad \frac{\partial^2 T}{\partial z^2} \ll \frac{1}{\alpha} \frac{\partial T}{\partial t} \quad [\text{Eq. 11}]$$

The authors reformulated these conditions for the thermal boundary condition of a step change in heat flux,

$$\frac{\partial^2 q}{\partial y^2} \ll \frac{q}{2\alpha t} \quad \text{and} \quad \frac{\partial^2 q}{\partial z^2} \ll \frac{q}{2\alpha t} \quad [\text{Eq. 12}]$$

and demonstrated that these conditions are routinely violated with the transient liquid crystal technique in the vicinity of 1.5 hole diameters downstream of the coolant injection point. Brauckmann and von Wolfersdorf [2005] employed a steady state IR technique to a shaped film cooling configuration and showed that a 3-D conduction model could be successfully employed to correct for the heat pick-up of the coolant fluid as it passes from the coolant plenum to the exit

orifice. Nirmalan et al. [2002] developed a procedure for non-destructively testing internal cooling passages of production turbine blades using a modified transient IR technique. IR images are taken of the external surface of a preheated blade subject to an instantaneously started internal coolant supply. Surface temperature distributions are used to estimate the internal passage heat transfer coefficient based on a 1-D lumped parameter model:

$$\frac{T_s(t) - T_{init}}{T_{coolant} - T_{init}} = \exp(-at) \quad \text{where } a = \frac{h_c}{\rho l c_p} \quad [\text{Eq. 13}]$$

This lumped thermal capacitance model is explicitly valid only for low Biot number ($Bi = h_c l / \kappa \ll 1$). Its application to this test case assumes that the thermal resistance to conduction through the turbine blade wall is negligible by comparison with the internal convective heat transfer in the coolant passage. It also neglects lateral conduction within the wall itself. Nirmalan et al. used the 1-D approximate solution as the initial condition for internal heat transfer coefficients in a 3-D ANSYS model of the turbine wall. Thus the final analysis does account for temperature variations through the wall thickness and lateral conduction. Nirmalan et al.'s solution technique continues iteratively until the surface temperatures predicted by the 3-D model match those measured by the IR camera. The authors reported an overall increase of 40% in predicted h_c inside the coolant passage for the 3-D model compared to the initial 1-D prediction.

Based on these results, it is anticipated that accounting for lateral conduction on rough surfaces may have a significant influence on transient IR measurements of heat transfer coefficient. To conduct a formal assessment, a structured rectilinear grid was adapted to a rough surface topology originally generated by Bons et al. [2006] shown in Fig. 2.

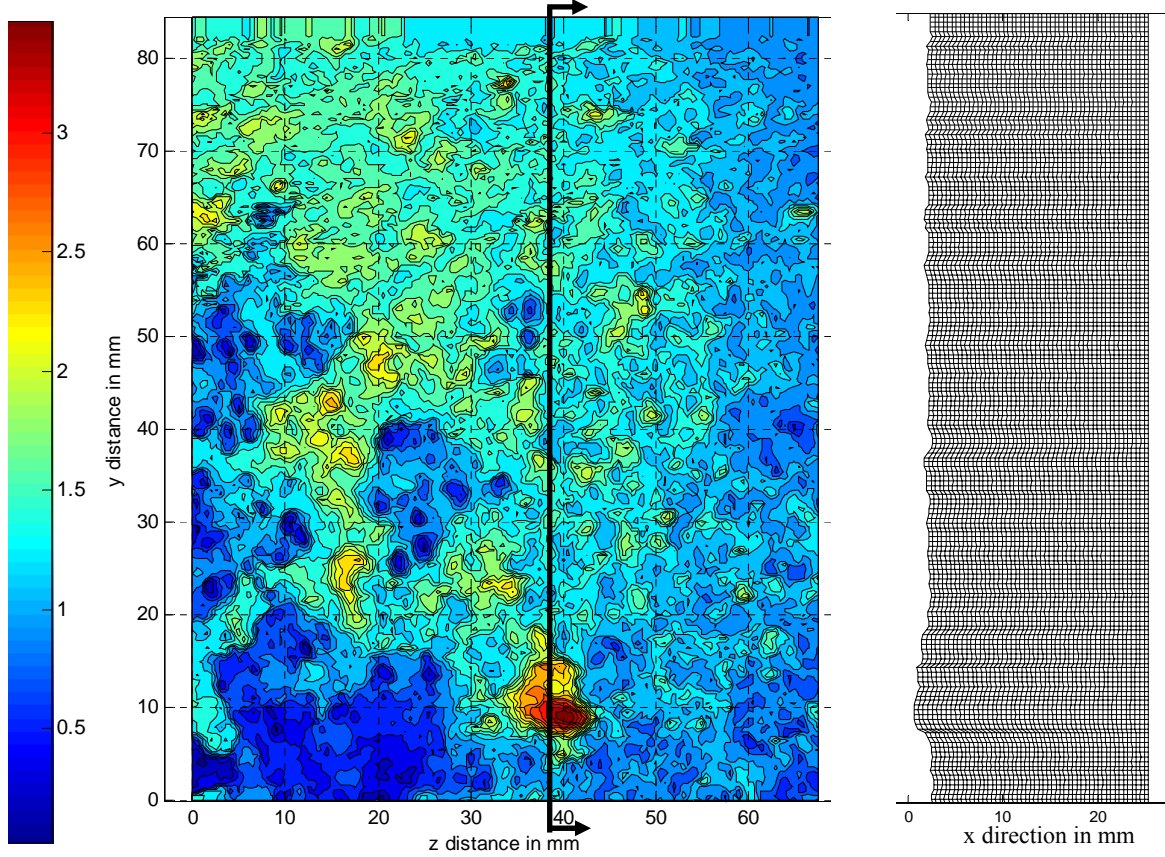


Figure 2: Rough surface topology showing slice of finite volume grid taken at $z = 38\text{mm}$.

As shown in Fig. 2, the lateral directions are y and z while the x -direction is into the solid. The largest roughness peak is approximately 3.5mm above the lowest valley for this topology. Cell temperatures are assigned to cell centers, allowing conservation of energy to be written for the (i,j,k) cell as follows:

$$V\rho c_p \frac{\partial T_{i,j,k}}{\partial t} = q_{x_{i,j,k}} A_{x_{i,j,k}} + q_{y_{i,j,k}} A_{y_{i,j,k}} + q_{z_{i,j,k}} A_{z_{i,j,k}} - q_{x_{i+1,j,k}} A_{x_{i+1,j,k}} - q_{y_{i,j+1,k}} A_{y_{i,j+1,k}} - q_{z_{i,j,k+1}} A_{z_{i,j,k+1}} \quad [\text{Eq. 14}]$$

For this study, the fluxes are discretized using a first-order approximation in space, e.g.

$$q_{x_{i,j,k}} \cong -\kappa \frac{T_{i,j,k} - T_{i-1,j,k}}{\Delta x_{i,j,k}} \quad [\text{Eq. 15}]$$

For the surface cell, the surface flux is approximated as,

$$q_{s_{1,j,k}} \cong -\kappa \frac{T_{1,j,k} - T_{s_{j,k}}}{0.5\Delta x_{1,j,k}} \quad [\text{Eq. 16}]$$

The temporal discretization is also approximated with a first order explicit formation,

$$\frac{\partial T_{i,j,k}}{\partial t} \cong \frac{T_{i,j,k_n} - T_{i,j,k_{n-1}}}{\Delta t} \quad [\text{Eq. 17}]$$

While other researchers have improved accuracy and processing time requirements by using higher order discretizations and more stable implicit formulations (e.g. Alternating Direction Implicit Method used by Ling et al., [2004]), the present algorithm was sufficiently stable to produce results in a reasonable timeframe for this study. The size of elements in the y and z-directions corresponded to the size of IR camera data pixels (roughly 0.5mm x 0.5mm). The rough surface topology necessitated a variable x-dimension for the 3-D cells, though the Δx cell size was held to within 16% of 0.5mm. For this size grid, stability was insured using a time step of 0.0625sec or smaller. Since the IR surface temperature data was acquired in 1sec intervals, the $T_s(y,z,t)$ maps were linearly interpolated in time to provide data at the smaller time step necessary for stability. The thickness of the roughness panel was 25.4 mm at its thickest point. It was fabricated from acrylic using a CNC mill as discussed in Bons et al. [2006]. The roughness topology is a 20 times scale model of roughness measured on a simulated gas turbine blade subjected to excessive deposition from ingested particulate. The topology was measured using a contact surface profilometer. The scaled surface was then milled with a conical countersink tool that matched the 90-degree cone shape of the profilometer stylus. The thermophysical properties, thermal conductivity (κ) and thermal diffusivity ($\alpha = \kappa / \rho c_p$), for the acrylic panel material were determined experimentally by Thermal Properties Research Laboratory (who incidentally employ a transient heat transfer technique). The measurements yielded the following values: $\kappa = 0.196 \text{ W/mK} \pm 6\%$ and $c_p = 1330 \text{ J/kgK} \pm 3\%$. The plastic density is $1188 \text{ kg/m}^3 \pm 2\%$.

Due to the low thermal diffusivity of the acrylic, test times shorter than five minutes yield a Fourier number ($Fo = \alpha t / l^2$) less than 1/16, which is the semi-infinite limit. This confirmed the use of the semi-infinite conduction assumption in the data processing. Thus, the back panel and sides of the 3-D finite-volume domain were prescribed with an adiabatic boundary condition. The present formulation did not account for property variations with temperature, though this refinement could be added through Eqs. 14-16.

Results and Discussion

The importance of lateral conduction can be illustrated by comparing the predicted $q_s(t)$ history for a 3-D finite volume analysis with that obtained using the 1-D approximate technique. Figure 3 shows $T_s(y,z)$ and $T_s(y,t)$ data taken on the roughness panel shown in Fig. 2 using a FLIR Thermacam SC 3000 IR camera. Figure 3(a) is the surface temperature map taken at $t = 50$ seconds. The panel was subjected to an instantaneous hot gas flow [$(T_\infty - T_{init}) \cong 23\text{K}$] at a time of $t = 3$ seconds as shown in the time history plot [Fig. 3(b)]. The flow direction was in the negative y -direction and the boundary layer was tripped turbulent, with a flow Reynolds number of 750,000. The boundary layer momentum thickness at the roughness panel was approximately 30% smaller than the maximum peak to valley height of the roughness (3.5mm).

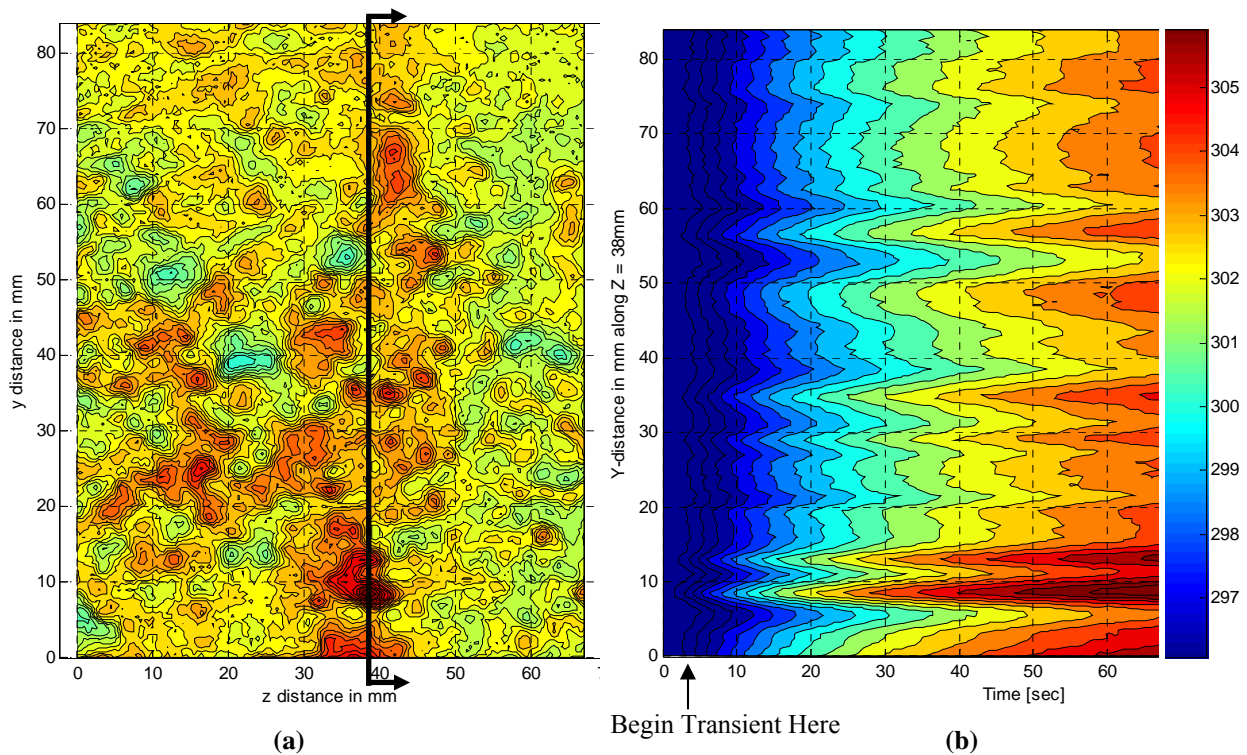


Figure 3: Surface temperature maps for rough surface measured with IR camera:

(a) $T_s(y,z)$ at $t=50$ sec and (b) $T_s(y,t)$ at $z=38$ mm. Temperatures in deg K.

The IR camera has a sensitivity of 0.03°C (at 30°C) and was focused on a 67 mm (crossstream) x 83 mm (streamwise) field of view. During testing, Bons et al. discovered that the infrared measurement was sensitive to the temperature of the surfaces surrounding the roughness panel. This occurred because some of the radiation that was incident on the camera originated from the wind tunnel enclosure and was reflected off the roughness panel. The

magnitude of this component of radiation varied as a function of the tunnel wall temperature. The FLIR software accounts for this by allowing the user to specify the ambient enclosure temperature. Since the heat transfer test was transient, this input was adjusted in post-processing to track the tunnel wall temperature as a function of time. Also, six 50 μm bead diameter thermocouples were flush mounted to the acrylic panel to verify the IR surface temperature measurement. This allowed calibration of the camera to within $\pm 0.3\text{C}$ of the initial surface temperature (T_{init}).

As expected, Figs. 3(a) and (b) show hot and cold spots at locations corresponding to peaks and valleys (respectively) on the surface topology map in Fig. 2. The roughness peaks exhibit a faster temperature response due to elevated convective heat transfer from the hot gas flow and higher air temperatures further from the wall in the thermal boundary layer. Figures 4(a) and (b) show time histories of the corresponding surface heat flux calculated using the 1-D and 3-D methods. The data are taken from the same $z=38\text{mm}$ slice as that shown in Fig. 3(b) for comparison. For purposes of illustration, the finite volume grid used to create the results shown in Fig. 4(b) was generated without the roughness topology. Thus, this result is for a “smoothed” surface and highlights the effect of lateral conduction only. The figures show that with time, the local q_s peaks become more pronounced in the 3-D result while they tend to fade with time in the 1-D analysis. This finding can be understood by revisiting the finite volume grid shown in Fig. 2. In the 3-D analysis, a local surface hot spot (e.g. due to a roughness peak) will create a higher temperature ($T_{1,j,k}$) cell just beneath the surface. This will in turn establish gradients for lateral heat flow to the cooler neighboring ($j\pm 1, k\pm 1$) cells. By conservation of energy, these lateral conduction losses must be offset by higher q_s from the surface. The 1-D heat flow model does not include these lateral “losses” and thus underpredicts the surface heat flux to the hot spots. Explained another way, to create the same hot surface temperature history a 3-D conduction model must impose a larger surface heat flux since a fraction of the heat absorbed by the solid surface is conducted laterally compared to the 1-D model where the only available path for heat flow from the surface is directly into the solid. A similar analysis shows the opposite trend for cold spots, for which the 1-D analysis over predicts the $q_s(t)$.

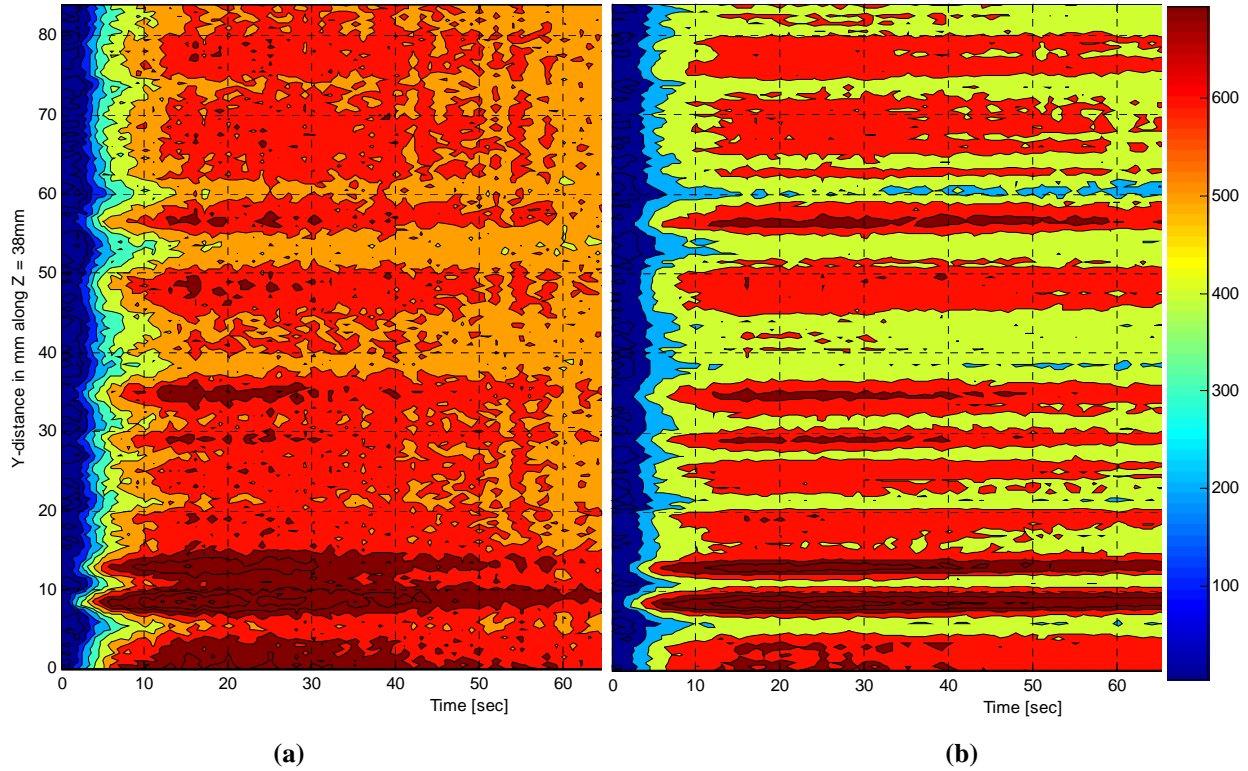


Figure 4: Contour maps of surface heat flux [W/m^2] time history for a “smoothed” surface: (a) $q_s(y,t)$ from 1-D approximate method and (b) $q_s(y,t)$ from 3-D finite volume method. Both plots at $z=38\text{mm}$.

The good news is that the area-averaged surface heat flux is identical for the two procedures. This result (shown in Fig. 5) is necessitated by conservation of energy for the solid. Since the surface has been “smoothed” in the 3-D solution, the surface area is the same for both methods and the area-averaged heat flux from the gas to the solid must be identical. Lateral conduction (except at the edges of the finite-volume domain) effectively redistributes the energy without losing any. Thus, underestimates of q_s on the hot spots are balanced by overestimates on the cold spots, resulting in the same spatially averaged heat flux measurement.

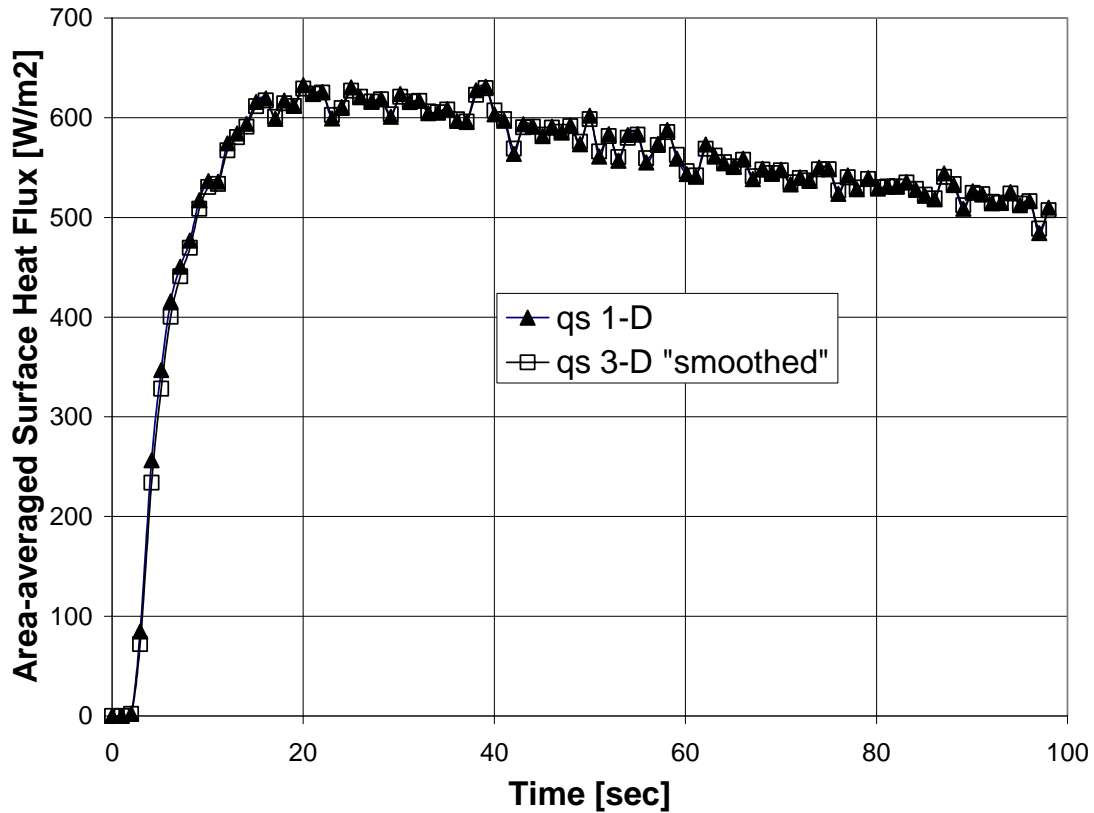
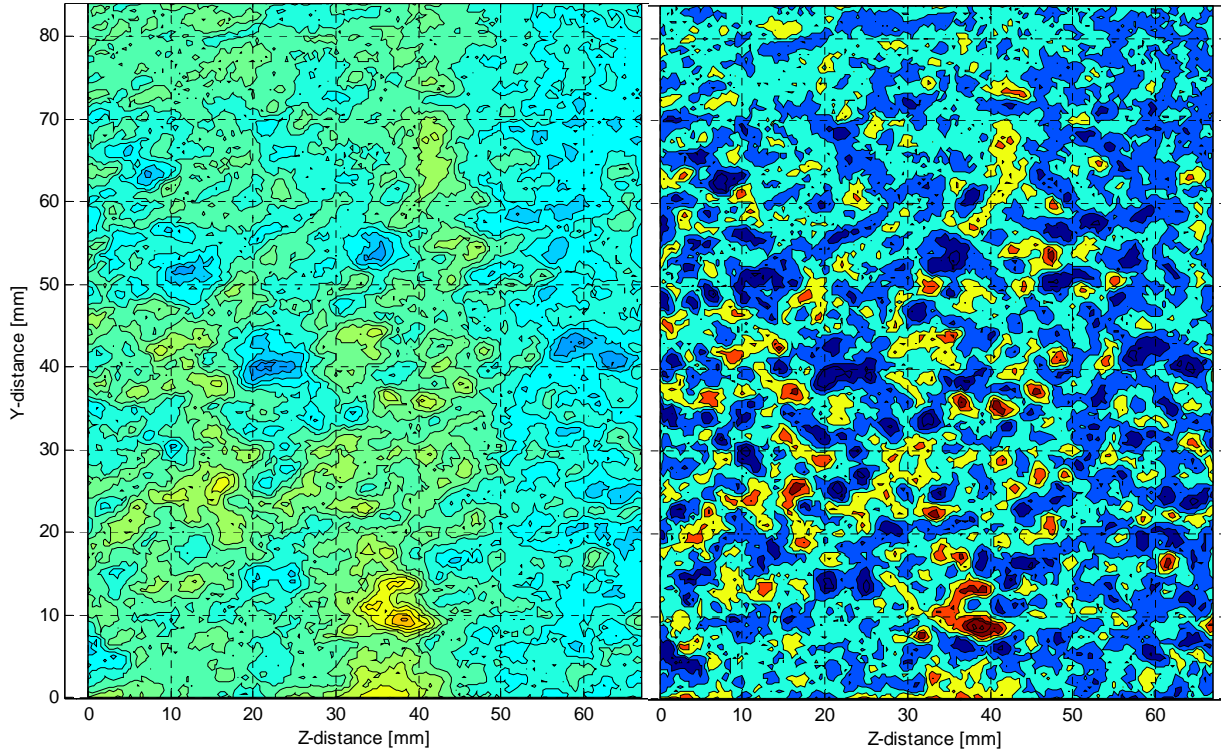


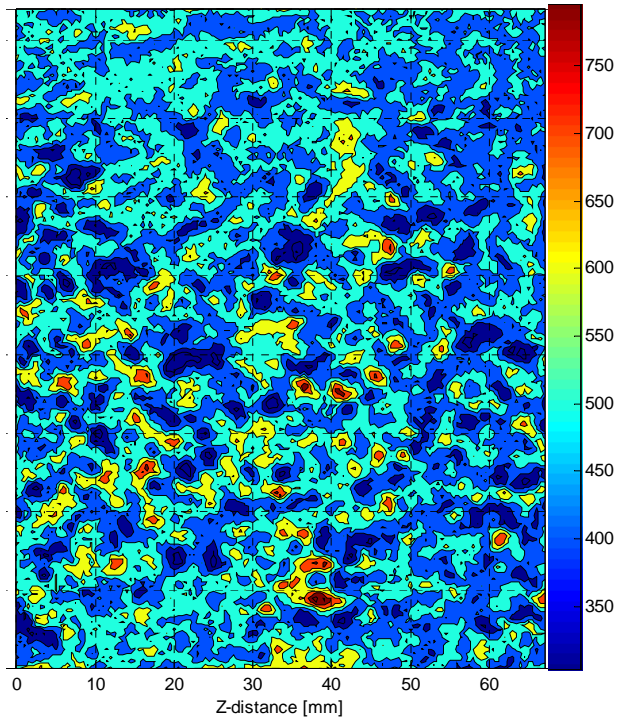
Figure 5: Area-averaged surface heat flux for 1-D approximate method vs. 3-D finite volume method for “smoothed” surface.

When the irregular surface topology is accounted for in the 3-D finite volume model, an unexpected result is produced. Figure 6 shows a comparison of the time-averaged $q_s(y,z)$ over the period of $80 < t < 100$ seconds. The contour plots show the results for three cases: (a) 1-D method, (b) 3-D method for “smoothed” surface, and (c) 3-D method for rough surface.



(a)

(b)



(c)

Figure 6: Time-averaged surface heat flux maps, $q_s(y,z)$ from: (a) 1-D approximate method, (b) 3-D method for “smoothed” surface, and (c) 3-D method for rough surface.

Lateral conduction still produces the effect of accentuating the predicted surface heat flux for hot spots and reducing the q_s for cold spots (compared to the 1-D analysis). The peaks in heat flux are less pronounced (by approximately 10%) in Fig. 6(c) compared to 6(b) due to the physical isolation of the peaks which effectively curtails the lateral conduction. Figure 7 plots a line of surface heat flux taken from each of the 3 contour maps in Fig. 6 (at $z = 38\text{mm}$). As noted in Fig. 6, the high points of q_s in Fig. 7 are always higher for the “smoothed” vs. the rough 3-D analysis while the low points are surprisingly lower for the fully rough analysis. This trend is even more evident in the area-averaged q_s time history plotted in Fig. 8 (note the smaller y-axis range compared to Fig. 5).

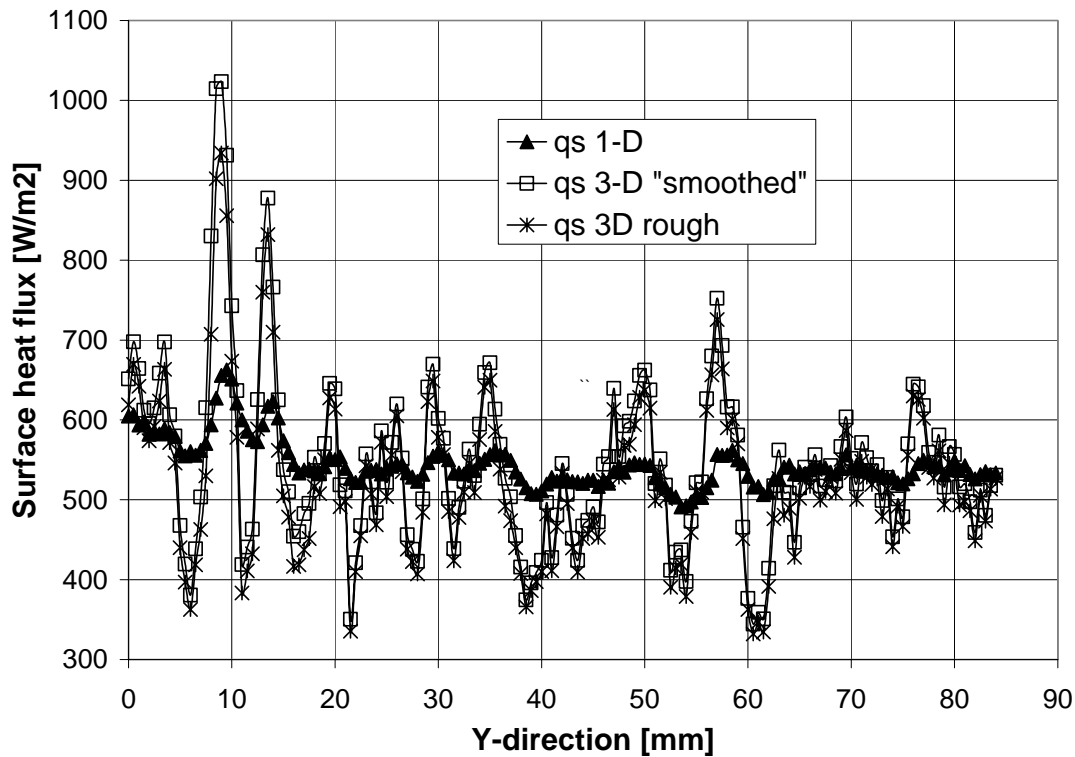


Figure 7: Time-averaged surface heat flux, $q_s(y)$ from: 1-D approximate method, 3-D method for “smoothed” surface, and 3-D method for rough surface. ($z=38\text{mm}$)

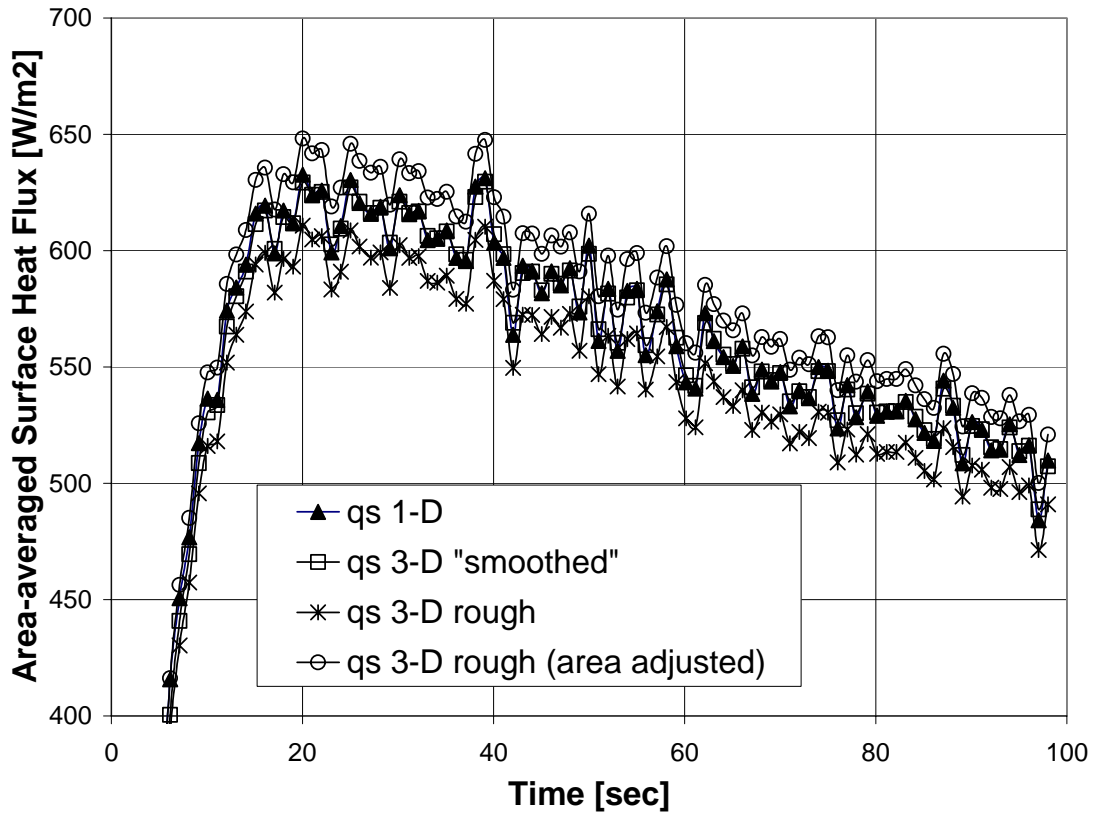


Figure 8: Area-averaged surface heat flux time history from: 1-D approximate method, 3-D method for “smoothed” surface, 3-D method for rough surface, and “area-adjusted” 3-D method for rough surface.

Unlike the result in Fig. 5 for the “smoothed” 3-D calculation, the area-averaged surface heat flux is now reduced from the value predicted by the 1-D approximate method. This result is unexpected since conservation of energy would seem to suggest that the area-averaging should even out the spatial variations in q_s due to lateral conduction (as it did for the “smoothed” geometry). However, the conservation of energy applies to the actual heat flux, Q , rather than the heat flux per unit area, q_s . When accounting for the irregular surface topology, the $T_s(y,z,t)$ history is imposed over a larger surface area than in the 1-D and “smoothed” cases (see schematic in Fig. 9). This contributes to a higher initial heat load ($Q=qA$) into each of the surface cells. This additional Q must still be conducted into the solid with the same thermal properties (α) as the 1-D method. Consequently, the additional Q gets bottled up in the first few cells near the surface and the rough surface finite-volume calculates a lower area-averaged $q_s(t)$ than the 1-D and “smoothed” 3-D models using the same $T_s(t)$ data. In essence, the temperature

of the first few layers of cells increases more rapidly due to the larger net Q in the rough surface model. Thus, it would take an even more rapid transient $T(t)$ rise to yield the same area-averaged q_s prediction as for the smooth surface. This explains why the predicted q_s on both the roughness peaks and valleys in Fig. 7 is less than the 3-D “smoothed” values.

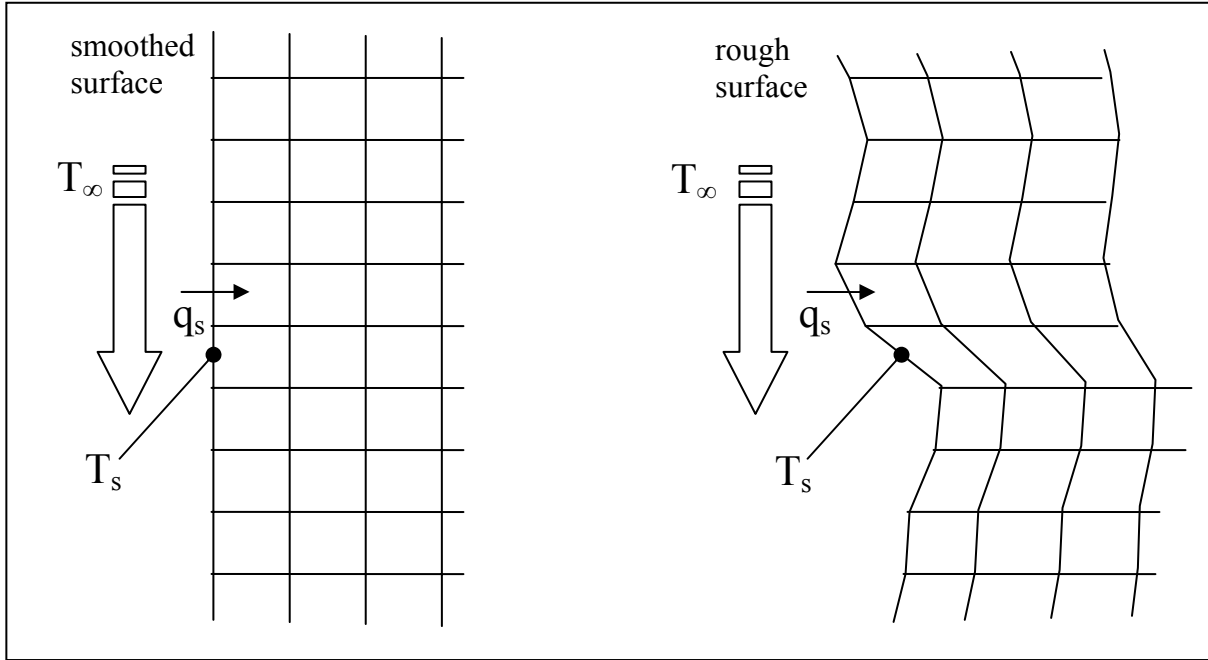


Figure 9: Schematic showing section of 3-D finite volume grid for “smoothed” surface vs. rough surface.

If the transient IR technique is used to obtain an area-averaged Stanton number for a rough surface to be compared with a corresponding smooth surface, the result in Fig. 8 suggests that appropriate precautions must be taken to make an accurate comparison. From an engineering perspective, the parameter of interest is usually the rate at which heat is absorbed by the solid rather than the “per unit area” heating. Unfortunately, Stanton number is based on the latter [$St = q_s / \rho c_p U_\infty (T_\infty - T_s)$]. Thus, the area-averaged St result from the transient 3-D conduction model should be multiplied by the ratio of wetted to planform surface area (S_{wet}/S_{flat}) to accurately account for the rate of heat transfer to the solid. For the rough surface representation employed in this study ($S_{wet}/S_{flat} = 1.063$), the difference is shown in Table 1. The “area-adjusted” St value predicts approximately 50% more heat transfer augmentation than does the unadjusted 3-D result for the rough surface compared to the smooth St value of 0.00228 for this Reynolds number (columns 2 and 3).

Table 1: Area-Averaged Stanton Numbers for Various Models. Data from 3 different roughness spatial resolutions (0.5, 1, and 2 mm). Time averaged data from $80 < t < 100$ sec.

Roughness Grid Spatial Resolution	0.5mm (matches IR camera)	0.5mm (matches IR camera)	1mm	1mm	2mm	2mm
	Area Averaged Stanton number	% St Increase from Smooth Plate St	Area Averaged Stanton number	% St Increase from Smooth Plate St	Area Averaged Stanton number	% St Increase from Smooth Plate St
Smooth wall result (from Bons et al.)	0.00228	0	0.00228	0	0.00228	0
Rough surface, 1-D	0.00265	16.2%	0.00265	16.2%	0.00265	16.2%
Rough surface, 3-D “smoothed”	0.00265	16.2%	0.00265	16.2%	0.00265	16.2%
Rough surface, 3-D	0.00257	12.7%	0.00261	14.5%	0.00263	15.4%
Rough surface, 3-D area-adjusted	0.00273	19.7%	0.00269	18.0%	0.00267	17.1%

Since the area-adjusted Stanton number for the rough surface in Table 1 is a function of the S_{wet}/S_{flat} ratio, the result depends on the spatial resolution of the surface roughness topology. The roughness panel employed in this study was milled from an acrylic sheet using a CNC mill with a data resolution of 0.4mm in both the y and z surface coordinates. This is very close to the 0.5mm spatial resolution of the IR camera used for the heat transfer measurement. To produce the topology map shown in Fig. 2, the raw height data used by the CNC mill was resampled at a 0.5mm resolution before being used in the finite-volume calculation. Thus the IR and surface topology maps are perfectly matched. If, however, the surface roughness data were on a coarser spatial grid than the IR camera resolution, the data could be interpolated to match the IR camera resolution. Of course, the interpolation process may not account for the true wetted surface area and could thus lose some of the accuracy of the local heat transfer spatial variation, thus affecting the area-averaged values. To demonstrate the magnitude of the effect of this interpolation process, the 0.5mm resolution surface height data were resampled at 1mm and again at 2mm spatial resolution. In each case, the coarse grid was then linearly interpolated back to the 0.5mm spatial grid to match the IR camera resolution. Doing so reduced the wetted surface area from $S_{wet}/S_{flat} = 1.063$ for the original (0.5mm resolution) surface, to $S_{wet}/S_{flat} = 1.033$ and 1.015 for the 1mm and 2mm resolution surfaces respectively. The corresponding

area-averaged results for Stanton number are shown in Table 1. As the wetted surface area decreases, both the “rough surface, 3-D”, and the “rough surface, 3-D area-adjusted” results converge to the “rough surface, 3-D smoothed” and “rough surface, 1-D” values. This is as expected since the process of linearly interpolating from a coarser and coarser mesh eventually approaches the “smoothed” limit.

For the data shown in Table 1, the spatial resolution of the roughness topology was equal to or coarser than the IR camera spatial resolution. It is perhaps more common that the IR spatial resolution would be more coarse than the surface topology variations. In this case, the IR camera will register a single average temperature for a region that may in fact be represented by multiple contiguous cell-faces in a finite volume representation. The lack of spatial resolution in the temperature map will produce the same “smoothing” effect that occurred from the coarser roughness height representations evaluated in Table 1. The area-averaged St will be underpredicted. Linearly interpolating the temperature data onto a finer grid will recover some, but not all of the lost measurement fidelity.

One additional roughness feature that must be considered when performing an optical surface temperature evaluation such as this is the surface angularity. When imaging a radiating surface at an angle other than normal ($\theta = 0$), the differential heat flux (dQ) incident upon a sensor in the optical image plane is related to the diffuse radiosity, I^+ , of the surface being imaged by

$$I^+ = \frac{dQ}{dA \cos \theta dw} \quad [\text{Eq. 18}]$$

(where dw is the differential solid angle). Thus, the radiated heat flux per unit area from the surface that is incident upon the sensor is,

$$q = \frac{dQ}{dA} = I^+ \cos \theta dw \quad [\text{Eq. 19}]$$

For illustration, a simplified schematic of the IR camera sensor array, camera optics, and a rough surface (2D representation only) are shown in Fig. 10. The IR sensor at location 2 receives an incident heat flux, dQ_2 , equal to $q_2 A_{\text{wet}2}$ radiated from the rough surface. From Eq. 19, $q_2 A_{\text{wet}2}$ is equal to $I_2^+ \cos \theta_2 dw A_{\text{wet}2}$ which is in turn equivalent to $I_2^+ dw A_{\text{flat}2}$ in this case since $\theta_2 = 0$ and $A_{\text{wet}2} = A_{\text{flat}2}$. Similarly for the sensor at location 1 which images the sloped surface element 1: $dQ_1 = q_1 A_{\text{wet}1} = I_1^+ \cos \theta_1 dw A_{\text{wet}1} = I_1^+ \cos \theta_1 dw A_{\text{flat}1} / \cos \theta_1 = I_1^+ dw A_{\text{flat}1}$. Since the $\cos \theta$ factor cancels in both cases, the temperature determined by the IR camera from the incident heat flux

(dQ) can appropriately be ascribed to the rough surface element, regardless of angularity (θ). This is true as long as the surface radiation obeys Lambert’s law, namely that the radiosity is independent of direction. Lambert’s law is derived for diffuse “gray” surfaces, but holds reasonably well for “real” surfaces up to a θ angle of 60 degrees. Beyond this, the directional emittance drops off appreciably [Mills, 1992]. Thus, optical surface heat flux measurement techniques are not suitable for rough surfaces with high surface angularity. For the surface used in this study, the maximum surface angularity was 62 degrees with a mean surface angle of 10.2 degrees. Also, a high surface emissivity is desirable since this reduces the percentage of surface radiation that is due to reflections from neighboring surface cells. The emissivity for the acrylic surface in this study was 0.9. Lower emissivity surfaces combined with high surface angularity will tend to smear out spatial temperature variations due to reflected radiation sensed by the IR camera.

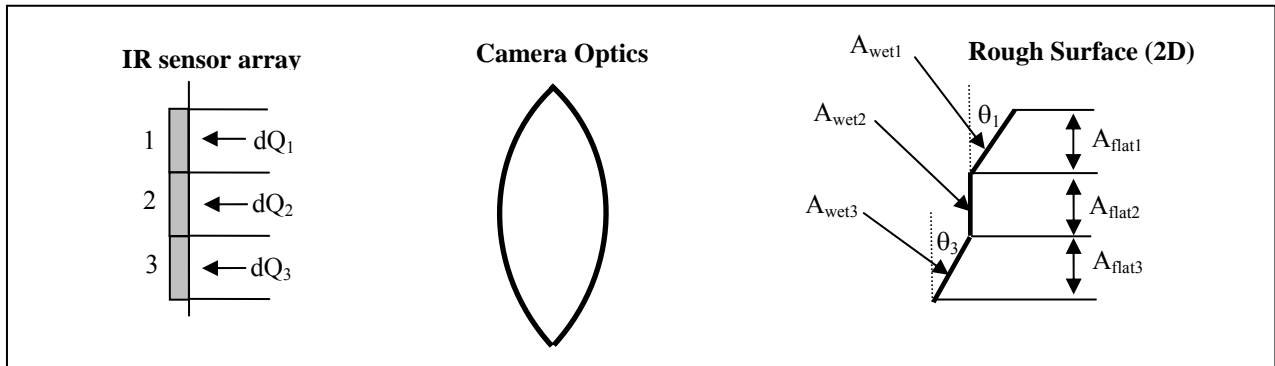


Figure 10: Schematic depicting optical imaging of rough surface onto IR sensor array.

Though the 3-D finite volume technique coupled with the transient IR method provides greater measurement accuracy, it does so at significant computational cost. Due to the smaller time step required for stability in the present implementation, the finite-volume method increases the computational time by a factor of over 500. Also, the 1-D method requires no detailed knowledge of surface topology, while the 3-D finite-volume method must have an accurate surface topology that is correctly positioned relative to the IR camera image. This added cost and complexity may not be warranted for the modest increase in accuracy for the area-averaged St measurements shown in Table 1. However, if accurate spatial resolution of St (or q_s) is desired, the images in Fig. 6 leave little doubt that the 1-D approximation method is not suitable.

For example in Fig. 7, both of the 3-D models show peak-to-valley excursions in predicted heat flux that are up to five times the corresponding amplitude predicted using the 1-D model. Thus, the effect of lateral conduction on the transient IR technique for this rough surface is very significant. Indeed, a survey of the 1-D assumption criteria shown in Eq. 11 shows that they are violated for over two thirds of the surface cells during the entire 100 second test window.

The above analysis and observations are true for the transient IR technique, but not the steady-state technique. In that case, there is no time-varying temperature distribution in the solid. Instead, the surface temperature is constant in time and represents a balance between the various heat transfer modes (conduction, radiation, and convection). In practice, guard heaters and insulation are employed to limit the conduction losses in the x-direction, and radiation losses are generally low (they were less than 1% of the convective heat transfer in the present study). If lateral conduction in the surface foil heater can be neglected due to its small thickness, the convective heat flux can be inferred directly from the surface foil heat generation per unit area and the measured surface temperature. If the surface is rough, the steady state technique will still yield the local convective heat flux assuming that the surface heating foil produces a uniform heat generation (even on roughness peaks). The optical surface temperature measurement will also be accurate provided that the angularity constraints are met. However, if the area-averaged Stanton number is desired, the “area-adjustment” shown in the last row of Table 1 is still warranted since the wetted surface area with roughness is larger than the projected or planform area of the surface.

Summary and Conclusions

The effect of lateral conduction on convective heat transfer predictions using the transient infrared technique over a rough surface is evaluated. Comparisons are made between a full 3-D finite volume analysis and a simpler 1-D transient conduction model. The randomly rough surface is a scaled model of actual surface deposits generated in a gas turbine flowfield. The surface temperature time history was measured with a high resolution infrared camera during an impulsively started hot gas flow over the rough test plate at a flow Reynolds number of 750,000. The boundary layer was turbulent with the peak roughness elements protruding just above the boundary layer momentum thickness. Based on the analysis, the following conclusions are made:

1. The 1-D model is not suitable for measurements of local surface heat flux (or St) around roughness elements. Neglecting lateral conduction can lead to a factor of five underestimate of the peak-to-valley variation of surface heat flux over the rough surface.
2. Care must be taken in making area-averaged St measurements of rough surfaces using optical methods. The wetted-to-flat surface area ratio (S_{wet}/S_{flat}) must be multiplied by the resultant area-averaged St from the 3-D model in order to properly account for the heat transfer augmentation due to roughness. If not, the error in predicted augmentation could exceed 50%. It is inaccurate to simply multiply the area-averaged St result from a 1-D analysis by the wetted-to-flat surface area ratio. This correction must only be performed with the 3-D model result. This conclusion is valid for both transient and steady-state measurement techniques.
3. For accurate surface heat flux prediction using the 3-D finite volume model, the spatial resolution of surface temperature should match that of the surface topology. If not, temperature smoothing and loss of wetted area can result in inaccurate predictions.
4. Surface angularity of the roughness elements must not exceed 60 degrees in order to assume a diffuse radiosity independent of direction.

In summary, transient St measurement over rough surfaces must be performed with significant care in order to produce accurate measurements of both local and area-averaged heat transfer.

Acknowledgements

The author would like to acknowledge several students who assisted in the collection of this data: James Wammack, Jared Crosby, and Daniel Fletcher. Drs. Brent Webb and Thomas Fletcher (both at Brigham Young University) contributed substantially to the analysis portion of this document. Their comments and encouragement are gratefully acknowledged.

References

- [1] Hosni, M.H., Coleman, H.W., and Taylor, R.P., 1991, "Heat Transfer Measurements and Calculations in Transitionally Rough Flow," *J Turbomachinery*, Vol. 113, July 1991, pp. 404-411.
- [2] Chen, P.H., and Goldstein, R.J., 1991, "Convective Transport Phenomena on the Suction Surface of a Turbine Blade Including the Influence of Secondary Flows near the Endwall," ASME paper 91-GT-35.
- [3] Gao, Z., Wright, L.M., and Han, J-C, 2005, "Assessment of Steady State PSP and Transient IR Measurement Techniques for Leading Edge Film Cooling," presented at IMECE 2005 in Orlando, FL, Nov. 5-11, 2005. IMECE2005-80146.
- [4] Powell, O.A., and Bons, J.P., 2001, "Heat Transfer To The Inclined Trailing Wall Of An Open Cavity," *AIAA Journal of Thermophysics and Heat Transfer*, July-Sept 2001, Vol. 15, No. 3, pp. 293-301.
- [5] Roger, M., 2007, "A Periodic Transient Method for High-Resolution Heat Transfer Measurement on Two-Dimensional Curved Surfaces. Part 1 – Theory," submitted to *J Heat Transfer*.
- [6] Bunker, R.S., 2004, "Latticework (Vortex) Cooling Effectiveness Part 1: Stationary Channel Experiments," presented at the 2004 IGTI in Vienna, Austria, June 14-17, 2004, GT2004-54157.
- [7] Nasir, H., Ekkad, S.V., Bunker, R.S., and Prakash, C., 2004, "Effects of Tip Gap Film Injection from Plain and Squealer Blade Tips," presented at the 2004 IGTI in Vienna, Austria, June 14-17, 2004, GT2004-53455.
- [8] Ou, S., and Rivir, R.B., 2006, "Shaped Hole Film Cooling with Pulsed Secondary Flow," presented at 2006 IGTI in Barcelona, Spain, May 8-11, 2006, GT2006-90272.
- [9] Nirmalan, N.V., Bunker, R.S., and Hedlund, C.R., 2002, "The Measurement of Full-Surface Internal Heat Transfer Coefficients for Turbine Airfoils Using a Non-Destructive Thermal Inertia Technique," *J Turbomachinery*, Vol. 125, pp. 83-89.
- [10] Walker, D.G., Scott, E.P., and Nowak, R.J., 2000, "Estimation Methods for Two-Dimensional conduction Effects of Shock-Shock Heat Fluxes," *J Thermophysics and Heat Transfer*, Vol. 14, No. 4, pp. 553-539.
- [11] Lin, M., and Wang, T., 2000, "A Transient Liquid Crystal Method Using Hue Angle and a 3-D Inverse Transient Conduction Scheme," presented at 2000 IGTI in Munich, Germany, May 8-11, 2000, 2000-GT-0231.
- [12] Bogard, D.G., Schmidt, D.L., and Tabbita, M., 1998, "Characterization and Laboratory Simulation of Turbine Airfoil Surface Roughness and Associated Heat Transfer," *Journal of Turbomachinery*, Vol. 120, No. 2, April 1998, pp. 337-342.
- [13] Hosni, M.H., Coleman, H.W., and Taylor, R.P., 1991, "Measurements and Calculations of Rough-Wall Heat Transfer in the Turbulent Boundary Layer," *Int J. Heat Mass Transfer*, Vol. 34, No. 4/5, pp. 1067-1082.
- [14] Mills, A.F., *Heat Transfer*, 1st Edition, 1992, Irwin, Illinois.
- [15] Kakac and Yener, *Heat Conduction*, 1st Edition, 1992, Taylor and Francis.
- [16] Cook, W.J., and Felderman, E.J., 1966, "Reduction of Data from Thin-Film Heat-Transfer Gages: A Concise Numerical Technique," *AIAA Journal*, Vol. 4, pp. 561-562.
- [17] Schultz, D.L. and Jones, T.V., 1973, "Heat-transfer Measurements in Short-duration Hypersonic Facilities," *Advisory Group for Aerospace Research and Development*, No. 165, NATO.

- [18] Brauckmann, D., and von Wolfersdorf, J., 2005, "Application of Steady State and Transient IR-Thermography Measurements to Film Cooling Experiments for a Row of Shaped Holes," presented at IGTI 2005 in Reno, NV, June 6-9, 2005, GT2005-68035.
- [19] Baldauf, S., Schulz, A., and Wittig, S., 2001, "High-Resolution Measurements of Local Effectiveness from Discrete Hole Film Cooling," *J. Turbomachinery*, Vol. 123, Oct 2001, pp. 758-765.
- [20] Ling, J.P.C.W., Ireland, P.T., and Turner, L., 2004, "A Technique for Processing Transient Heat Transfer, Liquid Crystal Experiments in the Presence of Lateral Conduction," *J. Turbomachinery*, Vol. 126, April 2004, pp. 247-258.
- [21] Bons, J.P., Wammack, J.E., Crosby, J., Fletcher, D.H., and Fletcher, T.H., 2006, "Evolution of Surface Deposits on a High Pressure Turbine Blade, Part 2: Convective Heat Transfer," presented at the 2006 IGTI conference in Barcelona, 8-11 May, 2006. Paper #GT2006-91257.